Article

Elastic and Inelastic Ground Deformation in Shanghai Lingang Area Revealed by Sentinel-1, Leveling, and Groundwater Level Data

Yanling Chen [1,*] **, Minyan Liao** [2] **, Jicang Wu** [3] **, Xiaobo Li** [1,4] **, Fuwen Xiong** [5] **, Shijie Liu** [3] **, Yongjiu Feng** [3] **and Xiaoya Wang** [1]

1   Shanghai Astronomical Observatory, Chinese Academy Sciences, Shanghai 200030, China; lxb@ief.ac.cn (X.L.); wxy@shao.ac.cn (X.W.)
2   Chongqing Institute of Geology and Mineral Resources, Chongqing 401120, China; 1810654@tongji.edu.cn
3   College of Surveying and Geo-Informatics, Tongji University, Shanghai 200092, China; jcwu@tongji.edu.cn (J.W.); liusjtj@tongji.edu.cn (S.L.); yjfeng@tongji.edu.cn (Y.F.)
4   Institute of Earthquake Forecasting, China Earthquake Administration, Beijing 100036, China
5   Shanghai Institute of Geological Survey, Shanghai 200072, China; xiongfuwen@sigs.com.cn
*   Correspondence: ylchen@shao.ac.cn

Abstract: Shanghai Lingang New City, located in the southeast corner of Shanghai, was constructed by land reclamation from 2002 to 2005, in an area where the geological structure is prone to subsidence over time. Firstly, we explore the spatio-temporal pattern of ground subsidence and its mechanism using the Persistent Scatterers Interferometric Synthetic Aperture Radar (PSInSAR) technique by processing 50 scenes of Sentinel-1A images acquired from May 2016 to May 2018. In order to assess the accuracy of PSInSAR derived deformation, we collect the first-class leveling data at two benchmarks located in the study area; the comparison between the two settlement indicates that the maximum difference is 1.93 mm and 2.9 mm, respectively, which validates the PSInSAR's high accuracy. We then obtain the skeleton release coefficients by the joint analysis of PSInSAR measurements and groundwater level data. Finally, we find that this coastal area has undergone both elastic and inelastic deformation from 2016 to 2018. The outcome shows that the combination of different techniques is conductive to understand the deformation mechanism of the aquifer system in these coastal areas, which is expected to be a valuable reference for ground subsidence monitoring and groundwater extraction management.

Keywords: ground deformation; PSInSAR; leveling; groundwater; Shanghai Lingang New City

1. Introduction

Land reclamation, as an important way to use coastal areas to expand land resources, has been conducted in many regions such as the Netherlands [1,2], the Hong Kong International Airport [3–5], Macau [6], Tianjin [7,8], and Shanghai Lingang New City [9–11], which is located in the southeast corner of Shanghai, China. Due to the compaction and consolidation of the soil layer and groundwater extraction, these areas suffer from ground subsidence, which raises potential risks to urban buildings, bridges, metro lines, and other infrastructures, even threatening people's lives. The monitoring of land subsidence, the estimation of water release coefficient of the aquifer, and the correlation analysis between land subsidence and groundwater in these areas provide an important basis for the study of subsidence mechanisms and the formulation and implementation of certain protective measures.

InSAR (Interferometric Synthetic Aperture Radar) time series analysis techniques–such as PS-InSAR (Persistent Scatterers-InSAR), SBAS-InSAR (Small Baseline Line- InSAR), TCP-InSAR (Temporarily Coherent Point Interferometric Synthetic Aperture Radar) [12,13],

DS interferometry (DSI) [14], and other InSAR techniques–have been proven to be efficient in monitoring ground subsidence and the relationship between land subsidence and groundwater changes. Galloway et al. used radar data collected from ERS-1 satellite to detect and quantify land subsidence caused by aquifer system compaction in the Antelope Valley, Mojave Desert, California [15]. Hoffmann et al. used ERS-2 satellite data to monitor land subsidence in the Antelope Valley and compared these data with repeatedly surveyed benchmarks [16]. Erban et al. collected L-band ALOS PALSAR data to measure the land subsidence rate in the Mekong Delta in Vietnam [17]. Matano et.al processed three SAR datasets of ascending and descending orbits acquired over the Campania coastal sectors from June 1992 to July 2010, which provided new insights into the spatial variability of vertical ground deformation (subsidence/uplift) of the Volturno River coastal plain [18]. Wang et al. used C-band Envisat ASAR data to investigate the rate and extent of coastal land subsidence in the Pearl River Delta in China [19]. Liu et al. detected subsidence in a coastal area by implementing the ultrashort-baseline TCPInSAR algorithm with high-resolution TerraSAR-X images acquired over Tianjin (close to Bohai Bay) in China [20]. Zhao et al. used ASAR (2007–2010), CSK (2013–2016), and Sentinel-1A SAR images (2015–2017) to obtain the ground deformation rate in coastal areas in Shanghai using InSAR techniques [21–23]. There are many research results of the application of PSInSAR in Shanghai [24–33]; most scholars have analyzed the subsidence of the Shanghai area with InSAR space technology and levelling data. In this paper, we involve various technologies including not only PS-InSAR and leveling, but also groundwater level measurements taken monthly that are used to cross-validate each other, establish the relationship between settlement and groundwater in the delta area, and further distinguish the deformation types. This is helpful to further understand the evolution of land compaction and consolidation in the land reclamation area.

In this paper, we adopted 50 scenes of Sentinel-1A images acquired from May 2016 to May 2018 to detect and process persistent scatterers (PS) in Shanghai Lingang New City using the Persistent Scatterers Interferometric Synthetic Aperture Radar (PSInSAR) technique. Then, we compared the displacement time series of these high coherence points with groundwater well data and leveling data using PSInSAR technology. Finally, we estimated the aquifer parameters at groundwater wells and analyzed the deformation characteristics and their geophysical mechanism.

2. Study Area

Lingang New City is located in the southeast corner of Pudong New District, Shanghai, China, where 60% of the land was constructed by reclamation between 2002 and 2005 [9–11]. It is about 75 km from the center of Shanghai and has a total area of 152.15 km^2. Most of the Lingang New City area was built by land reclamation. Its coastal zone–a frequent landing site of typhoons and storm surges–is vulnerable to a number of natural disasters. Factors such as the natural consolidation of mucky soil and the compression effect of the underground soil layer structure often cause ground subsidence in this area.

The geographical location of Shanghai Lingang New City is shown in Figure 1. The locations of two groundwater wells (W65, W66) and two leveling points (F65, F66) are marked with asterisks in Figure 1. The names W65 and W66 under these asterisks are abbreviations for groundwater monitoring wells. The names F65 and F66 are abbreviations for leveling monitoring points. Groundwater well W65 and leveling point F65 are located at the same place, and W66 and F66 are similarly in the same location.

Figure 1. The geographical location of Shanghai Lingang New City and the location of groundwater wells and leveling monitoring points (marked with asterisk).

As shown in Table 1, the aquifers of Shanghai include: the submerged aquifer (A0), first confined aquifer (A1), second confined aquifer (A2), third confined aquifer (A3), fourth confined aquifer (A4), and the fifth confined aquifer (A5). Weakly permeable layers include: the topsoil layer (B0), first weakly permeable layer (B1), second weakly permeable layer (B2), third weakly permeable layer (B3), fourth weakly permeable layer (B4), fifth weakly permeable layer (B5), and the sixth weakly permeable layer (B6). This is according to the hydrogeological profile of the Shanghai area, as shown in Figure 2; aquifers and weakly permeable layers are missing in some areas. The second, third, fourth, and fifth confined aquifers contain abundant groundwater resources and are the main targets for emergent groundwater exploitation. To explore the relationship between groundwater and ground subsidence in Shanghai Lingang New City, we mainly consider here the thickness changes of the fourth confined aquifer, as the first, second, and third confined aquifers are in a reverse relationship between the upper and lower soft soil layers and the fifth aquifer is rare in the Lingang area. The large thickness index of the third and fourth aquifer sand layer in Lingang New City indicates that the development of the sand layer may increase ground subsidence during exploitation, especially during unreasonable groundwater extraction. Otherwise, it will not lead to ground subsidence disasters [34]; that is, the cumulative thickness indicators of the fourth confined aquifer can reflect the abundance of groundwater resources, and the thickness changes can reflect the surface subsidence. We take the changes in the water levels of the fourth confined aquifer as the research object in this paper.

Table 1. The List of Hydrogeological Section.

Hydrogeological Section	Full Name	Short Name
Aquifers	Submerged aquifer	A0
	First confined aquifer	A1
	Second confined aquifer	A2
	Third confined aquifer	A3
	Fourth confined aquifer	A4
	Fifth confined aquifer	A5
Weakly permeable layers	Topsoil layer	B0
	First weakly permeable layer	B1
	Second weakly permeable layer	B2
	Third weakly permeable layer	B3
	Fourth weakly permeable layer	B4
	Fifth weakly permeable layer	B5
	Sixth weakly permeable layer	B6
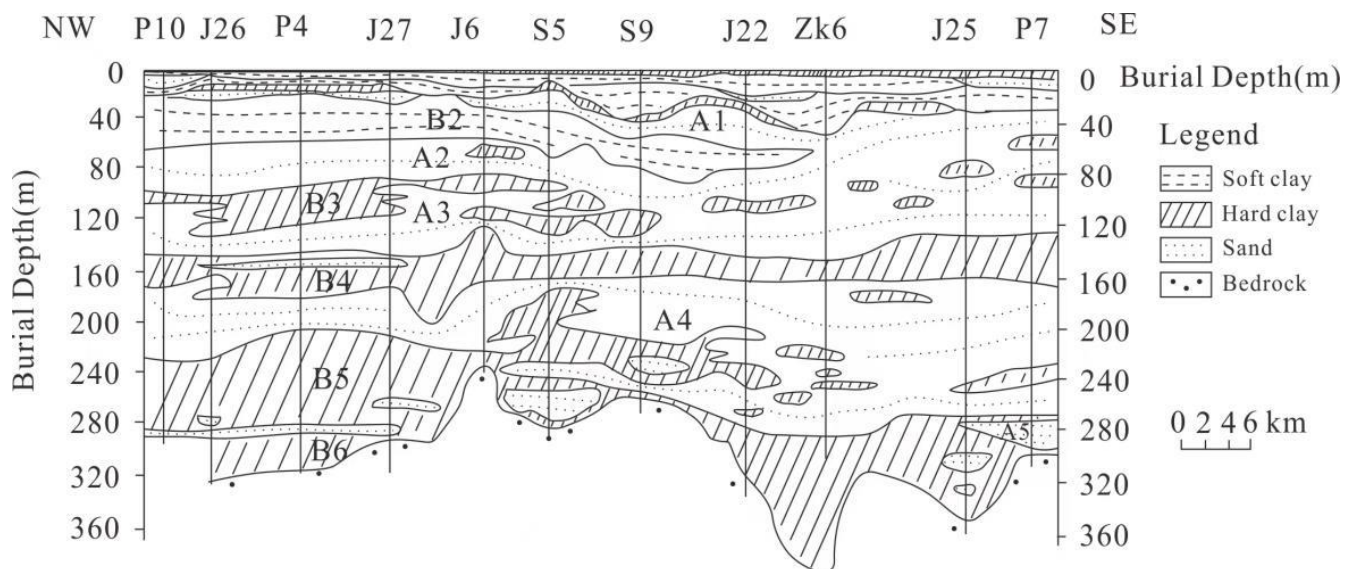
**Figure 2.** Hydrogeological Section Map of Shanghai City [34].

3. Materials and Methods

3.1. SAR Data

A total of 50 scenes of Sentinel-1A images acquired from 15 May 2016 to 5 May 2018 (seen in Table 2) are used to detect and process the high coherence points in Lingang New City, Shanghai. Figure 3 shows the distribution of the spatial and temporal baselines, where the image acquired on 27 June 2017 was selected as the reference image. In [35–38] the maximum temporal baseline was 408 days, and the maximum spatial baseline was 90 m. And thus the thresholds of temporal and spatial baselines were empirically set as 408 days and 90 m, respectively, to select interferograms.

Table 2. The List of SAR data and acquisition times.

No	Acquisition Time	No	Acquisition Time	No	Acquisition Time
1	20160515	18	20170311	35	20171013
2	20160608	19	20170404	36	20171106
3	20160726	20	20170416	37	20171118
4	20160819	21	20170428	38	20171130
5	20160912	22	20170510	39	20171212
6	20161006	23	20170522	40	20171224
7	20161018	24	20170603	41	20180117
8	20161030	25	20170615	42	20180129
9	20161111	26	20170627	43	20180210
10	20161123	27	20170709	44	20180222
11	20161205	28	20170721	45	20180306
12	20161217	29	20170802	46	20180318
13	20161229	30	20170814	47	20180330
14	20170122	31	20170826	48	20180411
15	20170203	32	20170907	49	20180423
16	20170215	33	20170919	50	20180505
17	20170227	34	20171001		
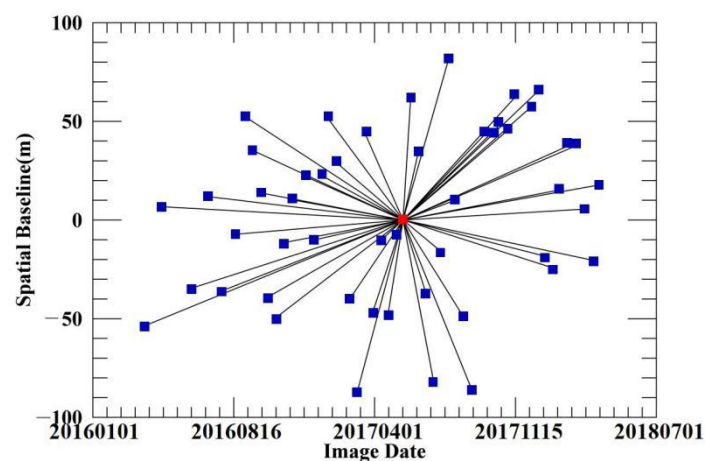
Figure 3. Distribution of the temporal and spatial baselines. The red square indicates the reference image; blue squares indicate the slave images.

3.2. Leveling Data

We collected the measurements from two first-class leveling points (i.e., F65 and F66, marked as asterisks in Figure 1) located in the study area to verify the accuracy of the InSAR measurements. The Trimble DINI03 digital level was used to obtain the leveling data with first-class leveling accuracy. The accuracy of the vertical displacement monitoring was ±0.3 mm. The F65 and F66 leveling points were observed monthly since 15 February 2011 and 25 February 2009, respectively.

3.3. Water Level Well Data

The Shanghai Institute of Geological Survey has conducted long-term monitoring of groundwater level changes in Shanghai. There are two groundwater level wells (W65, W66) in the study area, as shown in Figure 1, and the groundwater level is monitored monthly.

3.4. PSInSAR Technique

PSInSAR is an advanced InSAR technology that can accurately detect ground surface deformation from a stack of SAR images [39–43]. The PSInSAR technique has been widely used in urban areas with a high density of coherent points. This algorithm is a time series analysis method based on point targets with stable scattering characteristics (e.g.,

buildings, bridges, roads, and bare rocks). Then, time series analysis is performed on the interference phase to obtain high-precision surface observation information from these persistent scatterers.

When processing these SAR images, one SAR image is usually selected as the master image and the others are used as slave images. After registration and mitigation of the flattening effect, the external DEM (e.g., SRTM DEM 90 m × 90 m) is used to remove the topographic phase, and the differential interferograms are generated. Then, persistent scatterers (PS) that can keep high coherence in all the interferograms are selected. A Delaunay triangle network is generated from these PS points [44–48]. The wrap phase (φ_i^k) at the point i in the k th interferogram can be written as follows:

$$\varphi_i^k = W\left\{ \varphi_{i,def}^k + \varphi_{i,hgt}^k + \varphi_{i,orb}^k + \varphi_{i,atm}^k + \varphi_{i,noise}^k \right\} \tag{1}$$

where $W\{\cdot\}$ is the wrapping operator; $\varphi_{i,def}^k$ is the phase contributed by ground deformation, $\varphi_{i,hgt}^k$ is the phase associated with height errors, $\varphi_{i,orb}^k$ is the phase associated with orbital errors, $\varphi_{i,atm}^k$ is the phase that is related to the atmospheric delay, and $\varphi_{i,noise}^k$ is the noise.

The atmospheric phase and the orbit phase can be separated by temporal and spatial filtering. Finally, the time series deformation phase and average deformation rate of the line of sight of the satellite are obtained [49–53]. The deformation phase reflects the displacement of the ground during the observation time. SAR belongs to active remote sensing. The signal is measured twice from transmission to reception. Therefore, the phase change caused by ground point deformation can be expressed as:

$$\varphi_{i,def}^k = -\frac{4\pi}{\lambda} Def_{LOS} \tag{2}$$

where λ is the wavelength of the radar signal. Def_{LOS} is the deformation of the radar line of sight, and in the data analysis and comparison, it is necessary to transfer it to the vertical direction to compare it with levelling data or other vertical measuring data.

3.5. Reduction of InSAR Measurement

In order to investigate the relationship between ground deformation monitoring by PSInSAR and groundwater well observations, we processed them to the same scale by using the inverse distance square weighted (IDW) method, which has been widely used in many fields such as meteorological research, mine reserves research, oceans research, and other fields.

In this case study, the coherent points located within 100 m of the groundwater well and their subsidence time series were extracted. The deformation value of the groundwater well was calculated by the former IDW method for the coherent points. Then, the weighted deformation was seen as the surface deformation of the groundwater well within this time.

The weight function to calculate the weight of each PS point:

$$w_i = \frac{D_i^{-P}}{\sum_{i=1}^n D_i^{-P}} \tag{3}$$

where w_i is the weight of each PS point, D_i is the Euclidean distance between the PS point and the groundwater level point, P is the power parameter, and n is the number of PS point. In this paper, we use $P = 2$, which is the commonly used method of the inverse distance square weighted method.

Then, we use the inverse distance weighted function to obtain the estimated deformation value at the coordinates of the groundwater well:

$$Disp(h_0) = \frac{D_i^{-P} \sum_{i=1}^{n} Disp(h_i)}{\sum_{i=1}^{n} D_i^{-P}} \tag{4}$$

where $Disp(h_0)$ is the estimated deformation value of the groundwater well, $Disp(h_i)$ is the deformation value of the PS point.

Based on this method, the characteristics of the unknown geographic space are predicted.

3.6. Aquifer Parameters Estimation

According to the Terzaghi-Jacob theoretical model [54], the total stress of the confined aquifer (σ_T) is equal to the sum of the pore stress (p) and the effective stress (σ_e) of the aquifer.

$$\sigma_T = p + \sigma_e \tag{5}$$

When the groundwater in the confined aquifer is extracted, the groundwater level of the confined aquifer will decrease, resulting in the decrease of the pore stress and increase of the effective stress. The sum of these two stresses will introduce compression to the aquifer, which will cause ground subsidence.

When the effective stress of the aquifer σ_e is less than the historical effective stress $\sigma_{e(max)}$, the aquifer system undergoes elastic deformation, and the surface settlement can be recovered by measures such as recharging the groundwater. If the effective stress of the aquifer σ_e is continuously greater than the historical effective stress $\sigma_{e(max)}$, the aquifer system will undergo inelastic deformation, i.e., consolidation deformation, and the ground surface will have permanent ground subsidence.

The water release capacity of the confined aquifer is expressed by the water release coefficient. According to the Terzaghi-Jacob theoretical model, the relationship between the aquifer system deformation and groundwater level change can be represented by two different skeleton water release coefficients. Such coefficients are key hydraulic parameters for evaluating the water storage capacity of groundwater aquifer systems.

$$s_{ke}^* = \frac{\Delta b^*}{\Delta h}, \sigma_e < \sigma_{e(max)} \tag{6}$$

$$s_{ki}^* = \frac{\Delta b^*}{\Delta h}, \sigma_e > \sigma_{e(max)} \tag{7}$$

where s_{ke}^* is the elastic water release coefficient of the aquifer skeleton, s_{ki}^* is the inelastic water release coefficient of the aquifer skeleton, Δb^* is the deformation of the aquifer system obtained from the deformation results of PSInSAR, Δh is the change of groundwater level, which can be obtained by the change of groundwater level at the well.

When the aquifer thickness changes due to changes in the groundwater level, the actual observed water release coefficient can be compared with the theoretical value to determine whether the water release coefficient is elastic or inelastic. Therefore, whether elastic deformation or inelastic deformation occurs in the aquifer system can be determined.

4. Results and Discussion

4.1. PSInSAR Derived Deformation

Based on PSInSAR technology, the Sentinel-1A images covering Shanghai Lingang New City acquired from 15 May 2016 to 05 May 2018 were processed. The deformation rate map generated from 21,447 PS points is shown in Figure 4. PS points are mainly distributed on the west side of Dishui Lake in the experimental area. The deformation rate ranges from −67 mm/year to 1.1 mm/year in the LOS (line of sight) direction, and the average deformation rate is −3.4 mm/year in the LOS direction.
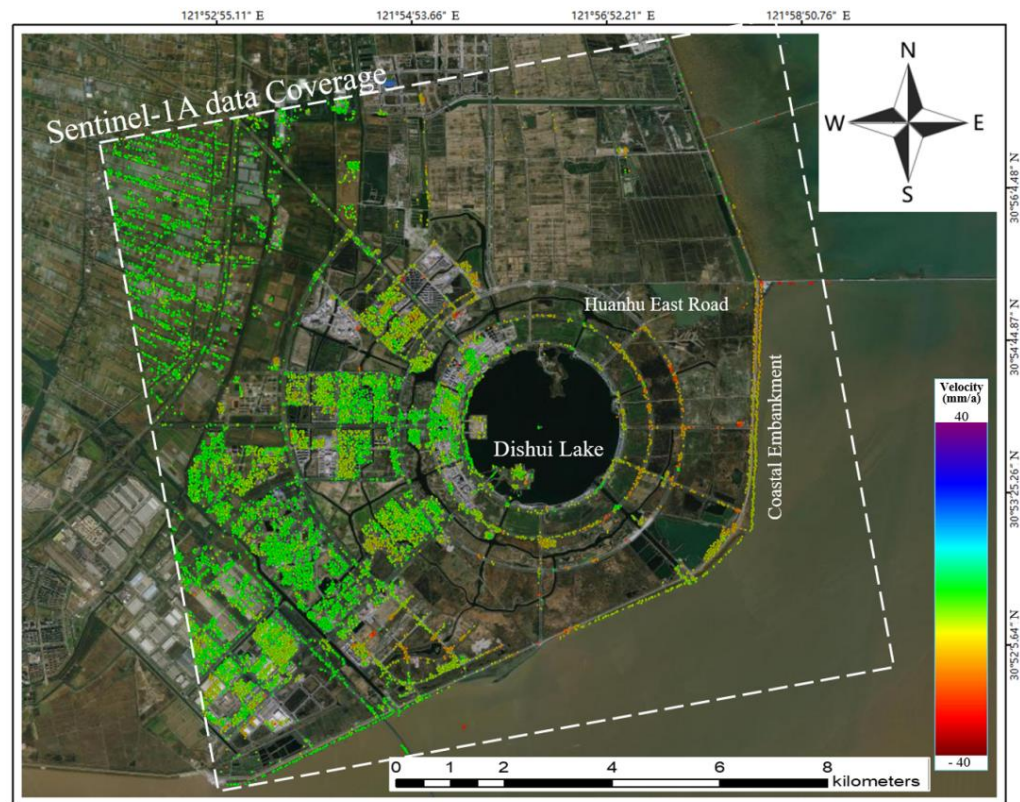
Figure 4. The map of the deformation rate map of Shanghai Lingang New City.

Dishui Lake is an artificial lake built on the beach in Lingang New City, the construction of which was started in 2002. The east and north sides of Dishui Lake are mainly farmlands and wetlands, where quite sparse PS points were identified. As shown in Figure 4, the area with large deformation is mainly concentrated on the east side of Dishui Lake. Although ground subsidence also occurred on the west side of Dishui Lake, it is relatively stable.

The coastal embankment on the east side of Dishui Lake suffered large subsidence, and notable subsidence also occurred around Huanhu East Road. Due to the late formation of land on the east side of Dishui Lake, such subsidence is mainly contributed by the compaction and consolidation of the soil layer in the area.

The coastal embankment, located on the east side of Dishui Lake in Shanghai Lingang New City, has a length of 4 km and was built on the beach with cement or bare rocks. The coastal embankment can help avoiding the erosion of the coast by external factors and is also an important guarantee for flood prevention. Figure 4 indicates the coastal embankment has larger deformation. To investigate the spatial pattern of the deformation, the PS points on the coastal embankment were extracted and their deformation rates were plotted in Figure 5. There are 334 PS points in total, and the density of PS points is about 85.6 points per kilometer. The deformation rate of the coastal embankment ranges from −18.23 mm/year to −4.69 mm/year in the LOS direction. The average deformation rate is −10.55 mm/year in the LOS direction. The statistics of the deformation rate of the coastal embankment from south to north is shown in Figure 6.
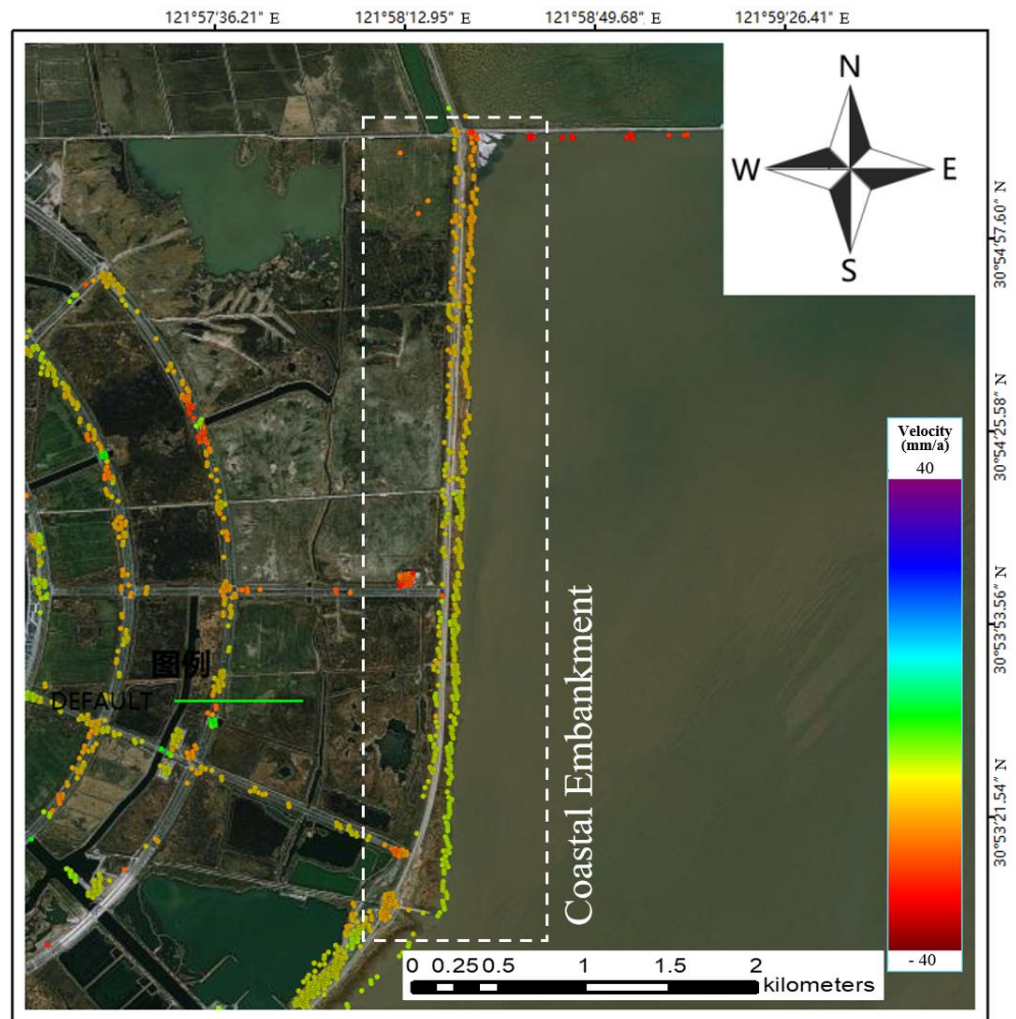
Figure 5. The deformation rate map of the coastal embankment.
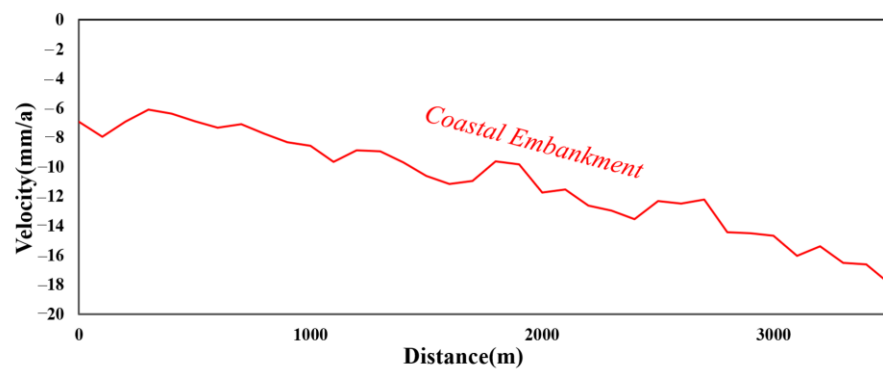

Figure 6. The statistics of the deformation rate in the LOS direction of the coastal embankment from south to north (x-axis is the distance from the coherence point to the starting point of the south).

The results show that the deformation rate on the north side of the coastal embankment is larger than that on the south side, see Figure 6. The deformation rate of the coastal embankment is continuous. Since there are no GPS measurements or leveling data on the coastal embankment section, the deformation results derived from InSAR technology provide useful data for the study of settlements in the area.

4.2. Analysis of Subsidence Characteristics and Leveling Verification

A comparison between the leveling observation data and the PSInSAR result at groundwater monitoring wells W65 and W66 is shown in Figures 7 and 8. Figure 7 shows the time series relationship between the leveling observation data F65 and the PSInSAR result at groundwater monitoring well W65. Figure 8 shows the time series relationship between the leveling observation data F66 and the PSInSAR result at groundwater monitoring well W66. InSAR results have been converted from the LOS direction to the vertical direction and then compared with the leveling data. The maximum difference of these two datasets at W65 and W66 is 1.93 mm and 2.9 mm, respectively. It indicates that the PSInSAR derived deformation time series has comparable accuracy with the leveling data. As the noise level at the selected PS points is similar, the deformation retrieved is expected to be reliable for exploring the geophysical mechanism behind the data.
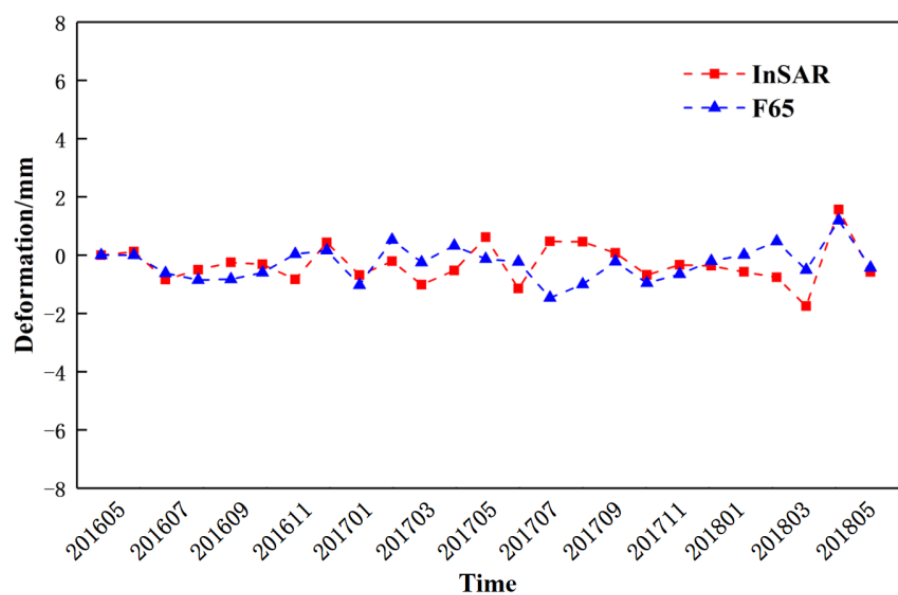

Figure 7. The time series relationship between the leveling observation data F65 and the PSInSAR result at groundwater monitoring well W65.
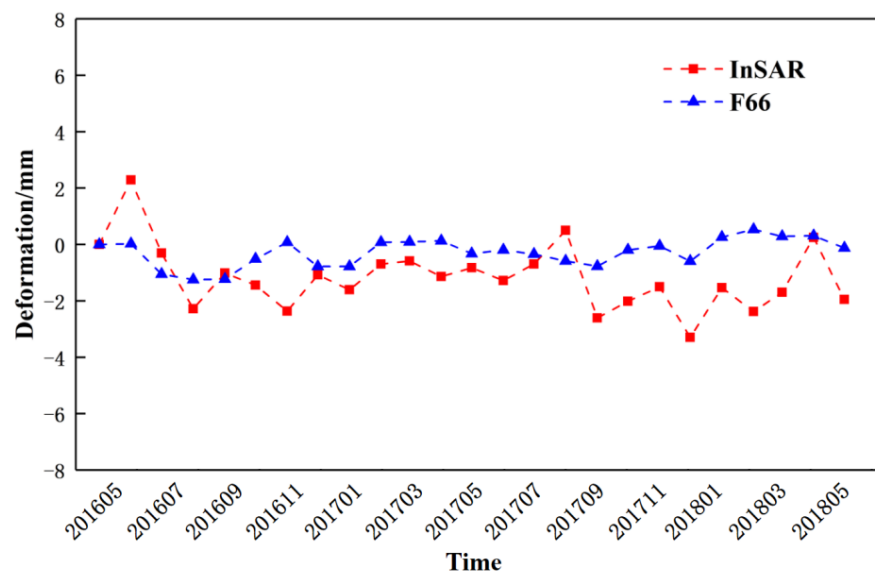
Figure 8. The time series relationship between the leveling observation data F66 and the PSInSAR result at groundwater monitoring well W66.

4.3. The Relationship between Groundwater Level Changes and Ground Subsidence

In order to study the ground subsidence of Shanghai Lingang New City and its mechanism, we used the groundwater level data at two monitoring wells (i.e., W65 and W66) to analyze the relationship between ground subsidence and groundwater level changes. The distribution map of groundwater wells is shown in Figure 1. The landscapes around these wells are shown in Figures 9 and 10. The groundwater monitoring well W65 is close to the coastline, surrounded by wasteland, houses, roads, and ponds. There was no new construction during our observation period. The W66 monitoring well is located on the west side of Hucheng Ring Road and is also near the river. This area is mostly occupied by farmlands.
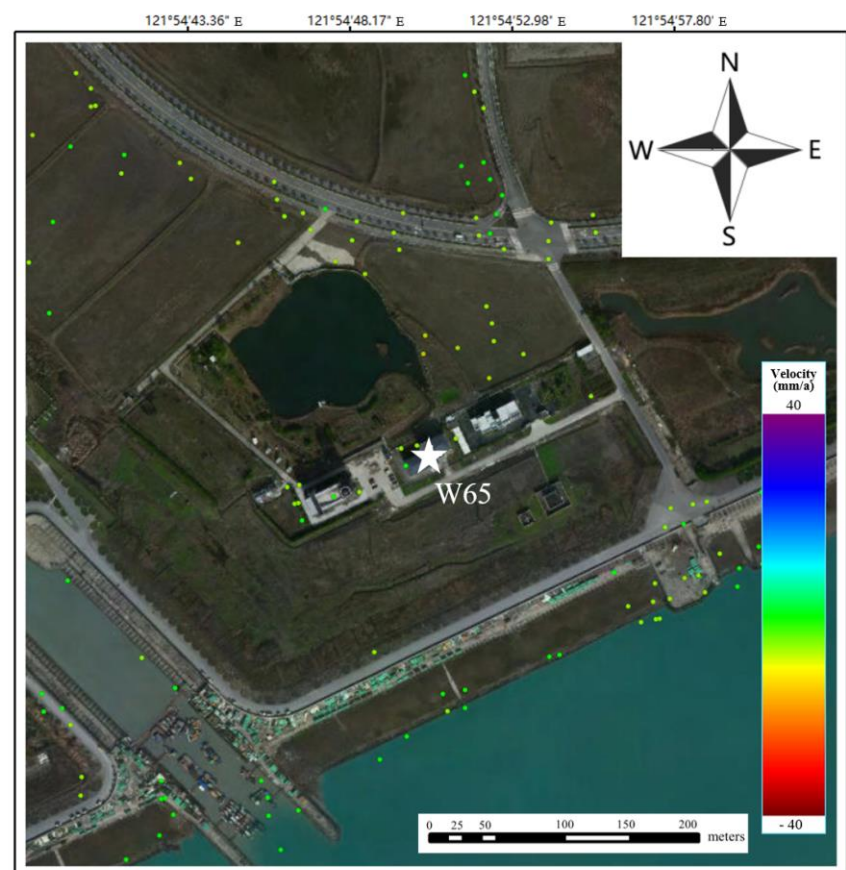
Figure 9. The distribution and deformation rate of PS points around groundwater well W65.

Figures 11 and 12 show the relationships between the groundwater level monitoring value of the fourth confined aquifer and the surface deformation obtained by the InSAR technique. During the observation period, the groundwater level of W65-4 (the fourth confined aquifer of groundwater monitoring well W65) varied within 2 m and had notable seasonal fluctuations. It is well documented that the groundwater level starts to rise in winter and spring and starts to decrease in summer and autumn. The ground deformation value obtained by the PSInSAR method at the monitoring well W65 is around 2 mm within two years, and the average deformation rate is −0.3 mm/year. The ground deformation trend is consistent with the variation of groundwater level data. The variation between InSAR results and groundwater level data had some relevance. It can be considered that it is stable relatively. On the other hand, during the observation period, the groundwater well level of W66-4 was quite steady before August 2017, and from August 2017 to May 2018 had undergone tremendous changes, but it still has the same deformation trend as the InSAR deformation results in the region.
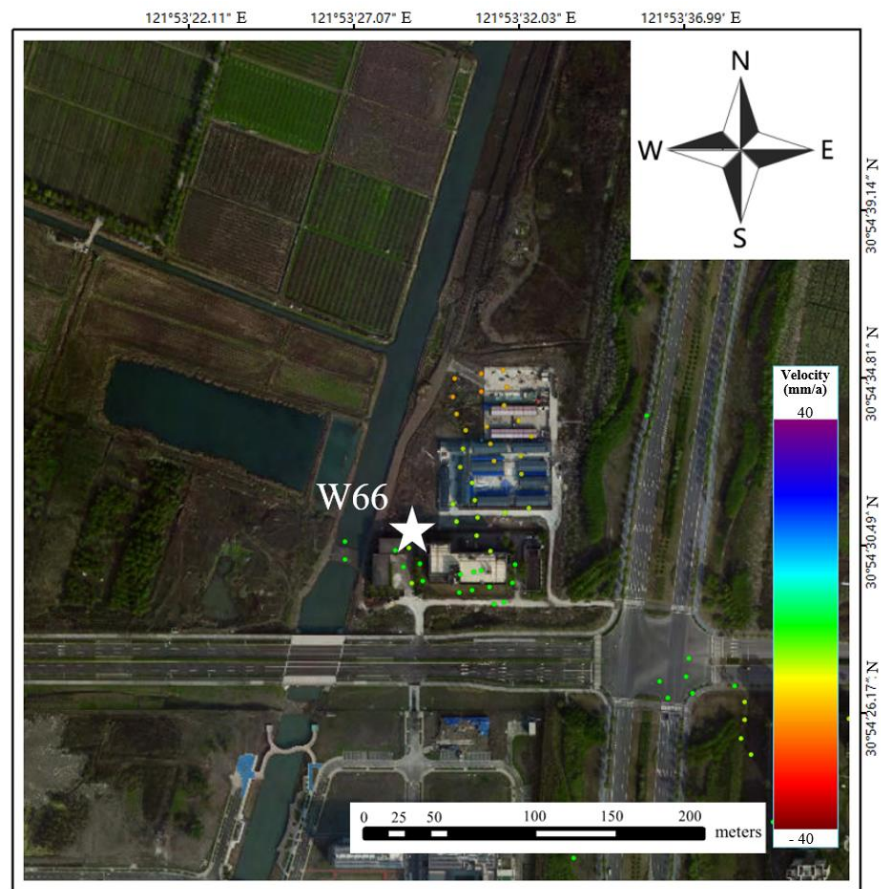
Figure 10. The distribution and deformation rate of PS points around groundwater well W66.
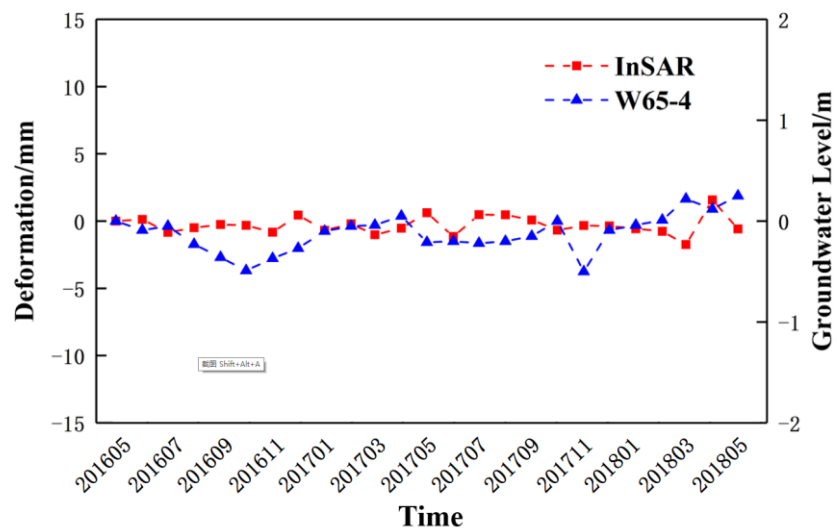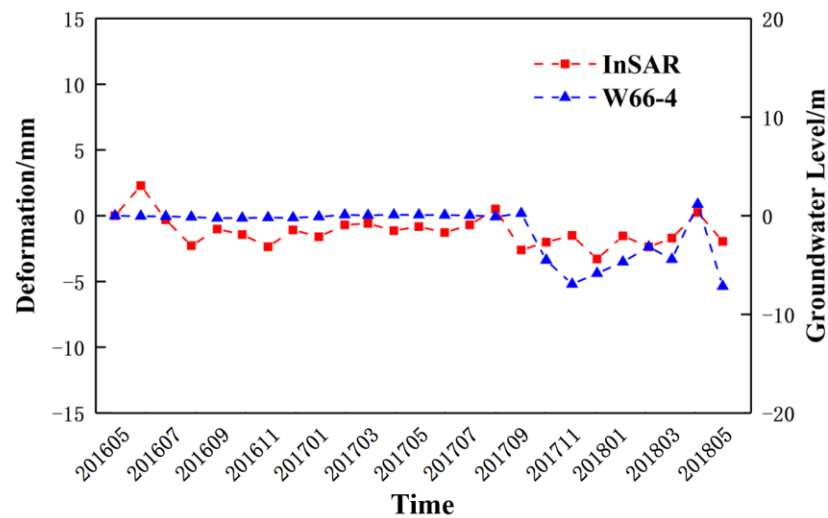

Figure 11. The relationship between PSInSAR derived deformation time series and groundwater level at well W65-4.

Figure 12. The relationship between PSInSAR derived deformation time series and groundwater level at well W66-4.

Table 3 shows elastic and inelastic skeleton release coefficients determined by PSInSAR deformation and groundwater level variations. W65 groundwater well skeleton release coefficient is between 0.0013–0.0087, and the correlation coefficient between PSInSAR deformation and groundwater level of W65-4 is 0.24 (positive correlation). Groundwater well skeleton release coefficient at well W66 is between 0.0024–0.0054, and the max correlation coefficient between InSAR deformation and groundwater level is 0.68 (positive correlation). According to the study conducted by Hoffmann in 2003 [55], the theoretical value of the elastic water release coefficient is generally between 10^{-5} and 10^{-3} for aquifers dominated by loose clay and silt, and the inelastic water release coefficient often reaches tens to hundreds of times the value of the elastic water release coefficient. Therefore, this indicates that the aquifer at the W65 well and W66 well had undergone elastic deformation.

Table 3. Elastic and inelastic skeleton release coefficients determined by InSAR deformation and groundwater level variations.

ID	Time Span (year/month)	Well (m)	InSAR (mm)	S^*_{ki}
W65-4	201605–201611	−0.37	−0.83	0.0022
	201611–201707	0.15	1.3	0.0087
	201706–201805	0.45	0.56	0.0013
W66-4	201605–201611	−0.19	−0.83	0.0044
	201611–201707	0.24	1.3	0.0054
	201706–201804	1.11	2.71	0.0024

4.4. Discussion

By using the Sentinel-1 A SAR images, leveling data, and groundwater well data, we have monitored the land subsidence in the delta area and reveal the geophysical mechanism behind this deformation.

In terms of the precision of PSInSAR vertical subsidence, the maximum difference of PSInSAR and leveling time series at two level points is 1.93 mm and 2.9 mm, respectively, which is basically consistent with Zhao et al.'s result that the mean of absolute difference values between COSMO-SkyMed and leveling measurements is 3.0 mm, and the mean difference value between Sentinel-1 A and leveling measurements is 3.6 mm; these data were obtained by studying Shanghai coastal deformation from February 2007 to April 2017 [21]. It validates that the PSInSAR derived deformation time series has millimeter-level comparable accuracy with the leveling data [32], which shows that the PSInSAR derived deformation is reliable for exploring the geophysical mechanism behind the data.

After extracting the settlement from the PSInSAR LOS deformation, we analyze the displacement of these PS points and the fluctuation of the two groundwater wells and confirm that the changes of the fourth layer confined aquifer data of Shanghai can better reflect the surface deformation in this area from 2016 to 2018. Previous research results related to the zone of the ocean-reclaimed lands of Shanghai are subject to subside due to soil consolidation and compression. Our results show that except for this reason, the settlement in our research of interest may be related to groundwater extraction. This was demonstrated by the comparative analysis of the PSInSAR settlement and groundwater level in the period from May 2016 to May 2018.

Furthermore, according to the Terzaghi-Jacob theoretical model [54], we determine the types of the ground subsidence near the coastal area in the delta by calculating skeleton water release coefficients, which shows that part of Shanghai Lingang New City suffered inelastic ground deformation; this type of deformation is difficult to recover and may result in secondary disasters [16].

The coastal embankment on the southeast side of Lingang New City suffered large subsidence, as shown through the PSInSAR from May 2016 to May 2018, which has been investigated in other period stages using ASAR, COSMO-SkyMed, and Sentinel-1 SAR images from February 2007 to April 2017 [21–23]. Its subsidence mechanism has not yet been fully studied due to lack of sufficient ground-truth validation, however this settlement should be taken seriously due to its special geographical location.

5. Conclusions

In this paper, we mainly used 50 scenes of Sentinel-1A images acquired from May 2016 to May 2018 to obtain the displacement time series of Lingang New City after 14 years' reclamation using the PSInSAR technique. By establishing the relationship between land subsidence and groundwater changes, we firstly combine ground in-situ observations such as first-class leveling data to validate the precision of PSInSAR, which indicates that the PSInSAR derived deformation time series has comparable accuracy with leveling data. Then, we integrate the groundwater well data to obtain the elastic and inelastic skeleton release coefficients, and finally obtain the type of deformation of this area.

The results show that the combination of multiple technologies is more conductive to understand the deformation mechanisms and fluctuation of aquifer systems in these coastal areas.

Therefore, we will next consider carrying out longer time series of SAR combined with ground monitoring to investigate the evolution of Shanghai Lingang New City for the management of coastal embankment safety risk assessment and adjustment, which is also extended to other case study areas.

Author Contributions: Conceptualization, Y.C., M.L. and J.W.; methodology, Y.C., M.L., J.W. and X.L.; software, Y.C., M.L. and X.L.; validation, Y.C., M.L., J.W., S.L., Y.F. and X.W.; data curation, M.L. and F.X.; writing—original draft preparation, Y.C., M.L., J.W. and F.X.; writing—review and editing, Y.C., M.L., J.W., X.L., F.X., S.L., Y.F. and X.W.; project administration, Y.C., M.L. and J.W.; funding acquisition, Y.C. and M.L. All authors have read and agreed to the published version of the manuscript.

Conflicts of Interest: The authors declare no conflict of interest.

References

1. Hoeksema, R. Three stages in the history of land reclamation in the Netherlands. *Irrig. Drain. J. Int. Comm. Irrig. Drain.* **2007**, *56*, S113–S126. [CrossRef]
2. Cuenca, M.C.; Hanssen, R.; Hooper, A.; Arikan, M. Surface deformation of the whole Netherlands after PSI analysis. In Proceedings of the Fringe 2011 Workshop, Frascati, Italy, 19–23 September 2011.
3. Zhao, Q.; Lin, H.; Gao, W.; Zebker, H.; Chen, A.; Yeung, K. InSAR detection of residual settlement of an ocean reclamation engineering project: A case study of Hong Kong International Airport. *J. Oceanogr.* **2011**, *67*, 415–426. [CrossRef]
4. Plant, G.; Covil, C.; Hughes, R. *Site Preparation for the New Hong Kong International Airport*; Thomas Telford: Telford, UK, 1998.
5. Liu, G.; Ding, X. Detecting of Surface Deformation in Coastlands by DInSAR: Accuracy and Applicability Analysis. *Bull. Surv. Mapp.* **2006**, *9*, 9–13.
6. Wan, X.; Hu, B.; Ma, Q. Monitoring ground subsidence in Macau with Persistent Scatters Interferometry. *Eng. Surv. Mapp.* **2012**, *21*, 39–43.
7. Luo, Q.; Perissin, D.; Li, Q.; Lin, H.; Duering, R. Tianjin INSAR time series analysis with L-and X-band. In Proceedings of the 2011 IEEE International Geoscience and Remote Sensing Symposium, Vancouver, BC, Canada, 24–29 July 2011; pp. 1477–1480.
8. Lv, X.; Niu, W.; Luo, L.; Zhang, Y.; Yi, N. Research on monitoring and control of land subsidence in a sea reclamation region of Tianjin. *Shanghai Land Resour.* **2016**, *37*, 55–59.
9. Zhang, J.; Hu, K.; Yue, W.; Liu, B.; Wang, J.; Gao, Q. Land Subsidence in Shanghai City and Its Response to Groundwater exploitation and reinjection. *Resour. Environ. Yangtze Basin* **2016**, *25*, 567–572.
10. Shen, S. Geological environmental character of Lin-Gang new city and its influences to the construction. *Shanghai Geol.* **2008**, *105*, 24–28.
11. Li, J.; Dai, Z.; Ying, M.; Wu, R.; Fu, G.; Xu, H. Analysis on the development and evolution of tidal flats and reclamation of land resource along shore of Shanghai city. *J. Nat. Resour.* **2007**, *22*, 361–371.
12. Zhang, L.; Ding, X.; Lu, Z.; Jung, H.; Hu, J.; Feng, G. A novel multitemporal InSAR model for joint estimation of deformation rates and orbital errors. *IEEE Trans. Geosci. Remote Sens.* **2013**, *52*, 3529–3540. [CrossRef]
13. Zhang, L.; Lu, Z.; Ding, X.; Jung, H.; Feng, G.; Lee, C. Mapping ground surface deformation using temporarily coherent point SAR interferometry: Application to Los Angeles Basin. *Remote Sens. Environ.* **2012**, *117*, 429–439. [CrossRef]
14. Wang, C.; Wang, X.S.; Xu, Y.; Zhang, B.; Jiang, M.; Xiong, S.; Zhang, Q.; Li, W.; Li, Q. A new likelihood function for consistent phase series estimation in distributed scatterer interferometry. *IEEE Trans. Geosci. Remote Sens.* **2022**, *60*, 5227314. [CrossRef]
15. Galloway, D.; Hudnut, K.; Ingebritsen, S.; Phillips, S.; Peltzer, G.; Rogez, F.; Rosen, P. Detection of aquifer system compaction and land subsidence using interferometric synthetic aperture radar, Antelope Valley, Mojave Desert, California. *Water Resour. Res.* **1998**, *34*, 2573–2585. [CrossRef]
16. Hoffmann, J.; Galloway, D.; Zebker, H. Inverse modeling of interbed storage parameters using land subsidence observations, Antelope Valley, California. *Water Resour. Res.* **2003**, *39*, 1031. [CrossRef]
17. Erban, L.; Gorelick, S.; Zebker, H.; Fendorf, S. Release of arsenic to deep groundwater in the Mekong Delta, Vietnam, linked to pumping-induced land subsidence. *Proc. Natl. Acad. Sci. USA* **2013**, *110*, 13751–13756. [CrossRef]
18. Matano, F.; Sacchi, M.; Vigliotti, M.; Ruberti, D. Subsidence trends of volturno river coastal plain (northern campania, southern italy) inferred by sar interferometry data. *Geosciences* **2018**, *8*, 1–22. [CrossRef]
19. Wang, H.; Wright, T.; Yu, Y.; Lin, H.; Jiang, L.; Li, C.; Qiu, G. InSAR reveals coastal subsidence in the Pearl River Delta, China. *Geophys. J. Int.* **2012**, *191*, 1119–1128. [CrossRef]
20. Liu, G.; Jia, H.; Nie, Y.; Li, T.; Zhang, R.; Yu, B.; Li, Z. Detecting subsidence in coastal areas by ultrashort-baseline TCPInSAR on the time series of high-resolution TerraSAR-X images. *IEEE Trans. Geosci. Remote Sens.* **2013**, *52*, 1911–1923. [CrossRef]
21. Zhao, Q.; Ma, G.; Wang, Q.; Yang, T.; Liu, M.; Gao, W.; Falabella, F.; Mastro, P.; Pepe, A. Generation of long-term InSAR ground displacement time-series through a novel multi-sensor data merging technique: The case study of the Shanghai coastal area. *ISPRS J. Photogramm. Remote Sens.* **2019**, *154*, 10–27. [CrossRef]
22. Zhao, Q.; Pepe, A.; Gao, W.; Lu, Z.; Bonano, M.; He, M.L.; Wang, J.; Tang, X. A DInSAR investigation of the ground settlement time evolution of ocean-reclaimed lands in Shanghai. *IEEE J. Sel. Top. Appl. Earth Obs. Remote Sens.* **2015**, *8*, 1763–1781. [CrossRef]
23. Zhao, Q.; Pepe, A.; Gao, W.; Li, X.; Lu, Z.; Bonano, M.; Manunta, M.; Lanari, R. Derivation of Ground Settlement Spatiotemporal Characteristics of Reclaimed Area in Nanhui New City, Shanghai, China, from Time-Series in InSAR Interpretation. *Dragon 3mid Term Results* **2014**, *724*, 39.
24. Luo, Y.; Yan, X.; Yang, T.; Ye, S.; Wu, J. Space-time characteristics of exploitation and recharge of groundwater and land subsidence if Shanghai land area. *J. Nanjing Univ. Nat. Sci. Ed.* **2019**, *3*, 449–457.
25. Yu, L.; Yang, T.; Zhao, Q.; Liu, M.; Pepe, A. The 2015–2016 ground displacements of the Shanghai coastal area inferred from a combined COSMO-SkyMed/Sentinel-1 DInSAR analysis. *Remote Sens.* **2017**, *9*, 1194. [CrossRef]
26. Zhang, K.; Yue, W.; Liu, B. Land Subsidence in Shanghai and Its Response to Groundwater Irrigation. *Yangtze River Basin Resour. Environ.* **2016**, *25*, 4.
27. Liao, M.; Pei, Y.; Wang, H.; Fang, Z.; Wei, L. Subsidence monitoring in Shanghai using the PSInSAR technique. *Shanghai Land Resour.* **2012**, *33*, 5–10.
28. Hu, S.; Wu, J.; Ban, B.; Zhang, L. PALSAR interferometry for urban subsidence monitoring: An experiment in Shanghai area. In Proceedings of the 2009 2nd Asian-Pacific Conference on Synthetic Aperture Radar, Xi'an, China, 26–30 October 2009; pp. 140–143.

29. Yang, M.; Jiang, Y.; Liao, M.; Wang, H. The analysis of the subsidence patterns in Lingang New City (Shanghai) using high-resolution SAR images. *Shanghai Land Resour.* **2013**, *34*, 12–16.
30. Shi, X.; Wu, J.; Ye, S.; Zhang, Y.; Xue, Y.; Wei, Z.; Li, Q.; Yu, J. Regional land subsidence simulation in Su-xi-Chang area and Shanghai City, China. *Eng. Geol.* **2008**, *100*, 27–42. [CrossRef]
31. Liu, G.; Luo, X.; Chen, Q.; Huang, D.; Ding, X. Detecting land subsidence in Shanghai by PS-networking SAR interferometry. *Sensors* **2008**, *8*, 4725–4741. [CrossRef]
32. Yang, M.; Yang, T.; Zhang, L.; Lin, J.; Qin, X.; Liao, M. Spatio-Temporal Characterization of a Reclamation Settlement in the Shanghai Coastal Area with Time Series Analyses of X-, C-, and L-Band SAR Datasets. *Remote Sens.* **2018**, *10*, 3291. [CrossRef]
33. Ding, J.; Zhao, Q.; Tang, M.; Calò, F.; Zamparelli, V.; Falabella, F.; Liu, M.; Pepe, A. On the Characterization and Forecasting of Ground Displacements of Ocean-Reclaimed Lands. *Remote Sens.* **2020**, *12*, 297. [CrossRef]
34. Qiu, J.; Li, X. *The Quaternary Strata and Sedimentary Environment of Shanghai City*; Shanghai Science and Technology Press: Shanghai, China, 2007.
35. Attema, E.; Davidson, M.; Snoeij, P.; Rommen, B.; Floury, N. Sentinel-1 mission overview. In Proceedings of the 2009 IEEE International Geoscience and Remote Sensing Symposium, Cape Town, South Africa, 12–17 July 2009; pp. I-36–I-39.
36. Panetti, A.; Torres, R.; Lokas, S.; Bruno, C.; Croci, R.; L'Abbate, M.; Marcozzi, M.; Pietropaolo, A.; Venditti, P. GMES Sentinel-1: Mission and satellite system overview. In Proceedings of the EUSAR 2012; 9th European Conference on Synthetic Aperture Radar, Nuremberg, Germany, 23–26 April 2012 ; pp. 162–165.
37. Rostan, F.; Riegger, S.; Pitz, W.; Torre, A.; Torres, R. The C-SAR instrument for the GMES sentinel-1 mission. In Proceedings of the 2007 IEEE International Geoscience and Remote Sensing Symposium, Barcelona, Spain, 23–28 July 2007; pp. 215–218.
38. Yague, M.; De, Z.; Prats-Iraola, P. Coregistration of interferometric stacks of Sentinel-1 TOPS data. *IEEE Geosci. Remote Sens. Lett.* **2017**, *14*, 1002–1006. [CrossRef]
39. Ferretti, A.; Prati, C.; Rocca, F. Permanent scatterers in SAR interferometry. *IEEE Trans. Geosci. Remote Sens.* **2001**, *39*, 8–20. [CrossRef]
40. Ferretti, A.; Prati, C.; Rocca, F. Nonlinear subsidence rate estimation using permanent scatterers in differential SAR interferometry. *IEEE Trans. Geosci. Remote Sens.* **2000**, *38*, 2202–2212. [CrossRef]
41. Massonnet, D.; Feigl, K. Radar interferometry and its application to changes in the Earth's surface. *Rev. Geophys.* **1998**, *36*, 441–500. [CrossRef]
42. Bert, M. *Radar Interferometry: Persistent Scatterers Technique*; Springer: Berlin/Heidelberg, Germany, 2006.
43. Hooper, A.; Segall, P.; Zebker, H. Persistent scatterer interferometric synthetic aperture radar for crustal deformation analysis, with application to Volcán Alcedo, Galápagos. *J. Geophys. Res. Solid Earth* **2007**, *112*, 1–12. [CrossRef]
44. Hooper, A.; Zebker, H.; Segall, P.; Kampes, B. A new method for measuring deformation on volcanoes and other natural terrains using InSAR persistent scatterers. *Geophys. Res. Lett.* **2004**, *31*, L23611. [CrossRef]
45. Tofani, V.; Raspini, F.; Catani, F.; Casagli, N. Persistent Scatterer Interferometry (PSI) technique for landslide characterization and monitoring. *Remote Sens.* **2013**, *5*, 1045–1065. [CrossRef]
46. Kampes, B.; Hanssen, R. Ambiguity resolution for permanent scatterer interferometry. *IEEE Trans. Geosci. Remote Sens.* **2004**, *42*, 2446–2453. [CrossRef]
47. Hanssen, R. *Radar interferometry: Data interpretation and error analysis*; Springer Science & Business Media: Berlin/Heidelberg, Germany, 2001.
48. Czikhardt, R.; Papco, J.; Bakon, M.; Liscak, P.; Ondrejka, P.; Zlocha, M. Ground stability monitoring of undermined and landslide prone areas by means of sentinel-1 multi-temporal InSAR, case study from Slovakia. *Geosciences* **2017**, *7*, 87–103. [CrossRef]
49. Crosetto, M.; Monserrat, O.; Cuevas-González, M.; Devanthéry, N.; Crippa, B. Persistent scatterer interferometry: A review. *ISPRS J. Photogramm. Remote Sens.* **2016**, *115*, 78–89. [CrossRef]
50. Colesanti, C.; Locatelli, R.; Novali, F. Ground deformation monitoring exploiting SAR permanent scatterers. In Proceedings of the IEEE International Geoscience and Remote Sensing Symposium, Toronto, ON, Canada, 24–28 June 2002; pp. 1219–1221.
51. Perissin, D.; Wang, T. Repeat-pass SAR interferometry with partially coherent targets. *IEEE Trans. Geosci. Remote Sens.* **2011**, *50*, 271–280. [CrossRef]
52. Hooper, A.; Bekaert, D.; Spaans, K.; Arıkan, M. Recent advances in SAR interferometry time series analysis for measuring crustal deformation. *Tectonophysics* **2012**, *514*, 1–13. [CrossRef]
53. Hooper, A.; Zebker, H. Phase unwrapping in three dimensions with application to InSAR time series. *JOSA A* **2007**, *24*, 2737–2747. [CrossRef]
54. Terzaghi, K. *Erdbaumechanik auf bodenphysikalischer Grundlage*; F. Deuticke: Leipzig, Vienna, 1925.
55. Hoffmann, J. The application of satellite radar interferometry to the study of land subsidence over developed aquifer systems. Ph.D. Thesis, Department of Geophysics, Stanford University, Stanford, CA, USA, 2003; pp. 1–211.